



# Transmission electron microscopy of unstained hybrid Au nanoparticles capped with PPAA (plasma-poly-allylamine): Structure and electron irradiation effects

Lionel C. Gontard<sup>a,\*</sup>, Asunción Fernández<sup>a</sup>, Rafal E. Dunin-Borkowski<sup>b</sup>, Takeshi Kasama<sup>c</sup>, Sergio Lozano-Pérez<sup>d</sup>, Stéphane Lucas<sup>e</sup>

<sup>a</sup> Instituto de Ciencia de Materiales de Sevilla (CSIC), 41092 Sevilla, Spain

<sup>b</sup> Ernst Ruska-Centre for Microscopy and Spectroscopy with Electrons and Peter Grünberg Institute, Forschungszentrum Jülich, D-52425 Jülich, Germany

<sup>c</sup> Center for Electron Nanoscopy, Technical University of Denmark, DK-2800 Kongens Lyngby, Denmark

<sup>d</sup> University of Oxford, Department of Materials, Parks Road, Oxford OX1 3PH, UK

<sup>e</sup> NARILIS – NAMur Research Institute for Life Sciences, Research Center in Physics of Matter and Radiation (PMR), Laboratoire d'Analyses par Réactions Nucléaires (LARN), FUNDP University of Namur, Belgium

## ARTICLE INFO

### Article history:

Received 12 May 2014

Received in revised form 11 June 2014

Accepted 12 June 2014

Available online 20 June 2014

### Keywords:

Poly-allylamine

Hybrid nanoparticles

Organic–inorganic nanoparticles

Transmission electron microscopy

EFTEM

Irradiation effects

## ABSTRACT

Hybrid (organic shell–inorganic core) nanoparticles have important applications in nanomedicine. Although the inorganic components of hybrid nanoparticles can be characterized readily using conventional transmission electron microscopy (TEM) techniques, the structural and chemical arrangement of the organic molecular components remains largely unknown. Here, we apply TEM to the physico-chemical characterization of Au nanoparticles that are coated with plasma-polymerized-allylamine, an organic compound with the formula  $C_3H_5NH_2$ . We discuss the use of energy-filtered TEM in the low-energy-loss range as a contrast enhancement mechanism for imaging the organic shells of such particles. We also study electron-beam-induced crystallization and amorphization of the shells and the formation of graphitic-like layers that contain both C and N. The resistance of the samples to irradiation by high-energy electrons, which is relevant for optical tuning and for understanding the degree to which such hybrid nanostructures are stable in the presence of biomedical radiation, is also discussed.

© 2014 Elsevier Ltd. All rights reserved.

## 1. Introduction

In the past decade, the study of hybrid nanoparticles (NPs) has become a major field of investigation in colloid and materials science and has led to a variety of applications, especially in nanomedicine (Bawarski et al., 2008). Hybrid organic–inorganic NPs that are capped with polymers and naturally occurring biomolecules are of great interest for targeting vascular, extracellular and cell surface receptors. Although the inorganic components of hybrid NPs can be characterized readily using conventional transmission electron microscopy (TEM) techniques, a knowledge of the structural arrangement of the surrounding organic components, which is required to establish a better understanding and control over NP synthesis and properties, remains largely unknown. This situation results, in part, from the fact that

soft materials have poor electron-optical image contrast and are sensitive to the ionizing radiation that is used in conventional TEMs (Egerton et al., 2004). The use of heavy-atom staining is an alternative approach (Chen et al., 2006), but it degrades spatial resolution and is difficult to control, while electron-beam-induced effects, such as heating, hydrocarbon contamination and charging, can affect the structures and stabilities of such samples (Martin et al., 2005; Libera and Egerton, 2010). To an extent, electron-beam-induced heating and contamination can be reduced by using cryogenic stages, while charging can be reduced by using conductive coatings. In some cases, core–polymeric–shell NPs have been characterized successfully using TEM (Kang and Taton, 2005; Li et al., 2009) and high-angle annular dark-field scanning TEM (HAADF-STEM) (Krivanek et al., 2010; van Schooneveld et al., 2010), but in general one must attempt to delay the onset of damage by using low-dose techniques (Malac et al., 2007), low accelerating voltages (Drummy et al., 2004), low specimen temperatures (Libera and Egerton, 2010) and, more recently, direct electron detection (Gontard et al., 2014a). Although phase plates for TEM, including more unusual suggestions such as laser-based phase plates based

\* Corresponding author.

E-mail address: [lionel.cervera@icmse.csic.es](mailto:lionel.cervera@icmse.csic.es) (L.C. Gontard).

on the Kapitza–Dirac effect (Müller et al., 2010), may provide a solution to some of these problems in the future, these technologies are currently either under development or still impractical for continuous use (Nagayama and Danev, 2008). Nevertheless, in conventional electron microscopes, damage of electrically insulating polymers is unavoidable, in part because free electrons in the specimen cannot compensate for radiation-induced free radicals on a timescale that is shorter than that required for other chemical processes to occur.

Here, we assess the application of different TEM techniques for the characterization of Au NPs that have amino functionalities. The NPs are synthesized using plasma vapor deposition of Au (cores) and allylamine (caps), resulting in the formation of plasma-polymerized-allylamine shells. Such capped nanoconjugates have been successfully covalently immobilized *via* an amide linkage to Cetuximab monoclonal antibodies (Marega et al., 2012). *In vivo* studies of the nanoconjugates demonstrated active tumor targeting, opening new possibilities for cancer treatment (Karmani et al., 2013).

Polymers (including plasma-poly-allylamine (PPAA)) consist largely of light elements, whose elastic interactions with highly energetic electrons are relatively weak, while inelastic (energy-loss) processes are relatively strong (Libera and Egerton, 2010). The relatively high fraction of inelastically scattered electrons for lighter elements in polymers provides an alternative source of contrast, by using electron energy-loss spectroscopy (EELS) for mapping local changes in composition and the distributions of phases without the need to use heavy-element stains. The versatility of this technique, which has been used to study multiphase polymer morphology in blends, composites and block copolymers, results from the fact that incident high-energy electrons can excite valence electrons, inter- or intra-band transitions or plasmons (collective longitudinal oscillations of valence or conduction band electrons). In aromatic polymers, a characteristic energy-loss peak at  $\sim 7$  eV has been assigned to an electronic  $\pi$ – $\pi^*$  transition (Li and Egerton, 2004). However, it can also result from electron irradiation due to hydrogen abstraction followed by a reaction between adjacent primary-chain carbon atoms. Surface plasmons in NPs, which feature in the sub-10-eV (optical) regions of EEL spectra, have been studied intensively as a result of their importance in plasmonics and biomedicine (Jain et al., 2007; Haridas et al., 2008). In contrast, there has not been an equivalent theoretical effort aimed at understanding bulk plasmons, which typically have energies above 10 eV.

The selection of inelastically scattered electrons that lie within a narrow energy range forms the basis of compositional mapping using either spectrum imaging or energy-filtered TEM (EFTEM). EFTEM core-loss imaging of C, N and O has been invaluable for providing microchemical and topochemical information about polymer films and composites (Du Chesne, 1999). However, for NPs, damage and contamination of the specimen by the electron beam results in uncertainty in the analysis of the signals and in a loss of resolution. Recent developments include the use of dedicated *in situ* plasma cleaning in the TEM for EFTEM C K-edge studies of hybrid Au@polymer specimens (Horiuchi et al., 2009). Although low-loss EFTEM in the surface plasmon range ( $<5$  eV) is now used intensively (e.g., Nelayah et al., 2009) the bulk plasmon range is much less explored because of the difficulty of data interpretation (Howie, 2003). However bulk plasmons can be used to create high-contrast images with high signal-to-noise ratios to distinguish between different carbonaceous materials (Hunt et al., 1995; Du Chesne, 1999; Daniels et al., 2003; Linares et al., 2009).

Here, we use aberration-corrected TEM and thin sample supports at room temperature to record both low-loss and core-loss EFTEM images of unstained Au NPs that are coated with PPAA, an organic compound with the formula  $C_3H_5NH_2$  (Moreau et al.,

2009). The sizes of the Au particle cores range between 1 and 10 nm, while the thicknesses of the organic shells are typically below 2 nm. We show that it is possible to obtain high spatial resolution physico-chemical information about the organic shells and discuss the applicability of bulk-plasmon EFTEM for imaging the shells with high contrast. We also discuss the effects of electron-beam-induced degradation in the context of the effects of biomedical radiation techniques on such NPs.

## 2. Methods

### 2.1. Specimen preparation

Several methods of capping Au NPs with PPAA have been devised, including aqueous-phase techniques (Sardar et al., 2007) and layer-by-layer deposition of polyelectrolytes (Gittins and Caruso, 2001; Masereel et al., 2011). Here, we used a gas-phase physical process that provides a method for NP production that is independent of the substrate. In order to produce large quantities of material, we repeated the deposition of several stacks of NaCl/Au/PPAA on a stainless steel substrate (3 in.). After depositing more than 30 of these stacks sequentially, the substrate was immersed in water in order to transfer the capped Au NPs (Au@PPAA) into solution thanks to the NaCl dissolution (Moreau et al., 2009). PPAA capping prevents aggregation and precipitation and is suitable for mAb labeling.

The procedure for the production of each stack was as follows. We used a PVD vacuum system from AJA International equipped with two magnetron sputtering sources (bottom up configuration). The chamber was pumped down to  $10^{-4}$  Pa prior to the process (turbomolecular pump). The specimen holder was electrically isolated from the chamber, and connected to a radiofrequency (RF) power supply (13.56 MHz). Gold nanoparticles were produced by using one magnetron gun equipped with a 99.99% gold target (2 in. diameter), powered in DC mode at 75 W and at 24 Pa for 2 s. This high pressure ensures gold NP formation. The final monolayer (ML) equivalent thickness was 0.5 nm. Once the sample was covered with Au NPs, PPAA functionalization took place thanks to an RF allylamine plasma impinging on the substrate holder at 10 W RF, 8 Pa for 20 s. The PPAA thickness was about 1 nm. The sample was then moved above the second magnetron gun equipped with a stainless steel crucible (2 in. diameter) filled with NaCl (Merck). NaCl deposition was carried out at 30 W RF, 13 Pa for 60 s for a total thickness of 30 nm. The procedure was then repeated about 30 times: the AJA system is fully automated and a recipe was setup to ensure repeatability from production to production.

### 2.2. Characterization

For TEM observation, a drop of the solution was deposited onto a thin C support film on a Cu TEM grid and dried in air. The supporting C films used in the present experiments were obtained from Ted Pella and had thicknesses of below 10 nm. Bright-field and high-resolution TEM images were acquired at 300 kV with an aberration-corrected FEI Titan field emission gun (FEG) TEM using a  $2048 \times 2048$  pixel charge-coupled-device (CCD) camera without binning and a typical acquisition time of 2 s. EFTEM images were acquired using a Gatan imaging filter (GIF) that had a measured energy resolution (full width at half maximum of the zero-loss peak) of  $\sim 1.2$  eV.  $1024 \times 1024$  pixel EFTEM images in the bulk plasmon range were acquired using  $2 \times$  hardware binning, a 4 eV energy-selecting slit, an acquisition time of 7 s and an edge onset energy of 27 eV. Core-loss EFTEM was used to identify elemental distributions of N using the three-windows method, whereby images are recorded using two pre-edge and one post-edge

window. The pre-edge images are used to subtract the background in the post-edge window, assuming a power law background of the form  $AE^{-r}$ , where  $A$  and  $r$  are fitting parameters and  $E$  is the energy loss.  $512 \times 512$  pixel N core-loss elemental maps were acquired using  $4 \times$  hardware binning, a 30 eV energy-selecting slit, acquisition times of 10 s, edge onset energies of 353, 383 and 416 eV and three-window background subtraction in Digital Micrograph software from Gatan. EEL spectra were acquired by operating the TEM in spectroscopy mode. A dispersion of 0.5 eV/channel was used and the spectra were processed using *Digital Micrograph* software from Gatan. Energy-dispersive X-ray spectroscopy (EDXS) was performed at 300 kV using a Tecnai F30 FEG TEM equipped with a windowless X-MAX Si drift detector from Oxford Instruments with a dispersion of 5 eV/channel and a 6  $\mu$ s pulse processing time. The sample was tilted by  $30^\circ$  and spectra were processed using *TIA* software from FEI Company.

Atomistic models of core-shell NPs were generated using a dedicated software program written in *Matlab*. The shell was modeled by starting from a hypothetical  $C_3N$  crystal (with the correct C/N ratio for PPAA) comprising a face centered cubic structure with one C atom at each corner of the unit cell and a N atom at the center of each face. The unit cell dimension was chosen to be 0.2 nm, so that the average distance between the C and N atoms corresponds to the typical bond length expected in amines ( $\sim 0.148$  nm). In order to model an amorphous shell, the crystalline position of each atom was changed from its starting position by a random number multiplied by 20% of the unit cell dimension. This model was refined by deleting outer atoms selectively until the shape of the shell resembled that observed in experimental images. A hole was then created in the center of the shell to accommodate a Au NP. High-resolution TEM images were simulated using the multislice algorithm in *JEMS* software, with the transfer function of the microscope (defocus +90 nm; defocus spread 20 nm; beam convergence semi-angle 2 mrad) chosen to provide a match to the experimentally observed contrast and 1% random noise added to the final simulations. The large defocus used in the experimental images and

simulations is a reflection of the fact that contrast enhancement of the shells around the NPs is needed.

Casino v3.2 software was used to perform Monte Carlo simulations of inelastic electron scattering events and trajectories (Demers et al., 2011). In the simulations, which were performed with 100 electrons and parallel illumination, spherical 5 nm Au NPs were semi-buried in  $10 \text{ nm}^3$  of amorphous C.

### 3. Results

Fig. 1a shows a conventional BF TEM image of the Au@PPAA NPs supported on ultrathin C. The field of view is 300 nm and the dark particles of different size correspond to the Au cores. Shells are visible around the larger particles. The two main sources of contrast in BF TEM images are mass-thickness and diffraction contrast. The shells have uniform intensity irrespective of their size, suggesting that they are amorphous. Fig. 1b–d shows representative results of chemical analysis performed by averaging EDXS and EELS signals over an area of the specimen similar to that shown in Fig. 1a. The EDX spectrum in Fig. 1a confirms the presence of N but also indicates the presence of Si. The latter peak may be an artifact originating from the windowless Si detector. Fig. 1c shows an EEL spectrum of the core-loss N K-edge (401 eV) and O K-edge (532 eV), while Fig. 1d shows a corresponding spectrum of the C K-edge (284 eV). The N peak is the primary signature of the presence of allylamine ( $C_3H_5NH_2$ ) in the specimen. Although pristine allylamine contains single C–N bonds, sharp N and O edge onsets may indicate the presence of C=O and C=N groups (Garvie and Buseck, 2004). Such groups may form during the plasma discharge when the precursor (allylamine) is dissociated into fragments of different mass containing C–C, C–N, C–H and N–H bonds. The breaking of N–H bonds can lead to the formation of C=N groups during recombination. PPAA coatings may also oxidize in ambient air, resulting in the formation of C–O and C=O bonds due to polymer oxidation (Massey et al., 2010).

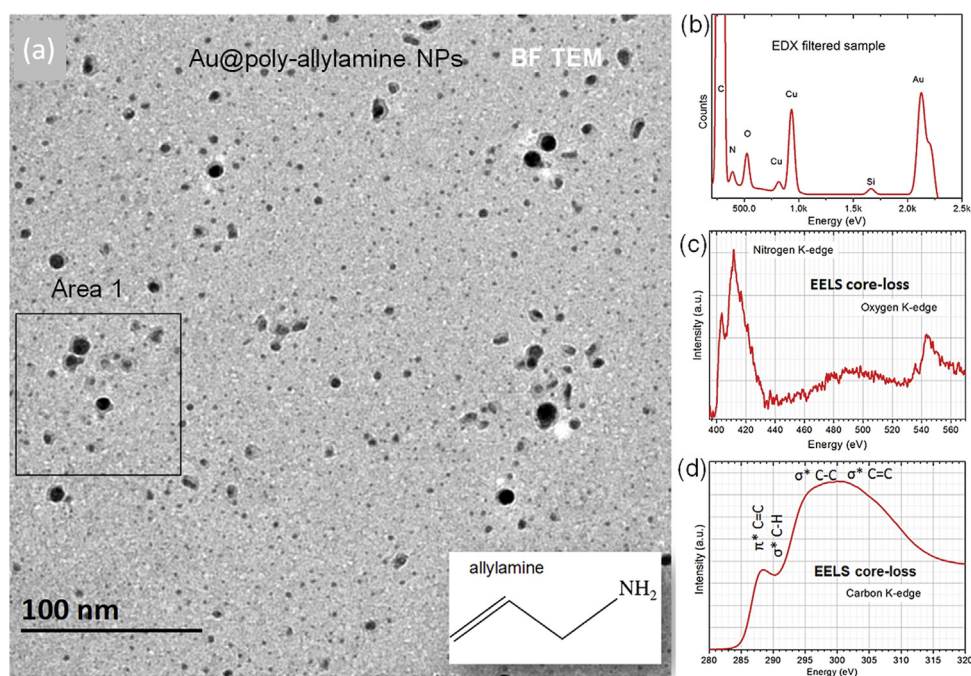


**Fig. 1.** (a) Bright-field TEM image of hybrid Au nanoparticles capped with allylamine supported on ultrathin (approx. 10 nm) amorphous C acquired after an electron dose exposure of  $250 \text{ C/cm}^2$ . The Au cores (darker) are surrounded by shells of lower density (lighter). The shells do not enclose larger particles completely. (b) EDX spectrum showing peaks of N, Au and a small amount of Si. (c) Core-loss EEL spectrum showing N and O K-edges. (d) Core-loss EEL spectrum showing the C K-edge. The strong Cu peaks originate from the grid bars of the TEM Cu grid.

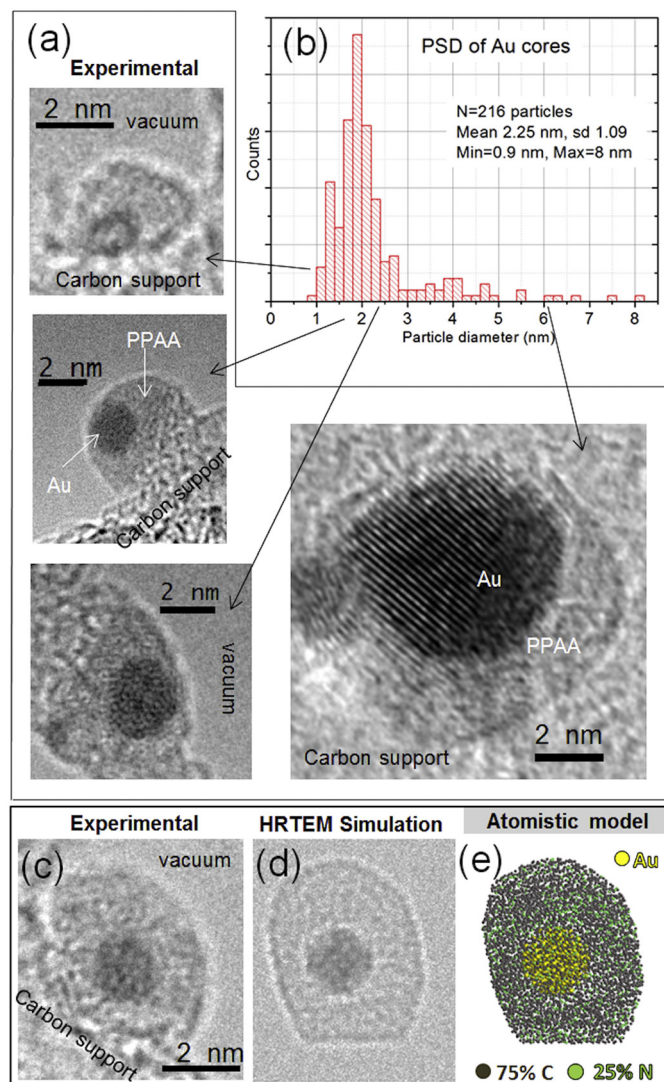
The C K-edge in Fig. 1d is similar to that expected for amorphous C, with the loss of structural order resulting in a relaxation of the selection rules for the  $1s$  to  $\sigma^*$  transition and producing a broad featureless peak at 290–310 eV. The spectrum contains two strong peaks at 288.5 and 300 eV, corresponding to  $C=C \pi^*$  and  $C=C \sigma^*$  bonds (Garvie and Buseck, 2004). The  $\pi^*$  to  $\sigma^*$  ratio can be calculated by assigning energy losses of 282–291 eV to  $\pi^*$  states and energy losses of 294–301 eV to  $\sigma^*$  states in the background-subtracted C K-edge spectrum shown in Fig. 1d. We obtain a value for the  $\pi^*/\sigma^*$  ratio of 0.4, suggesting a lack of long-range order (Katrinak et al., 1992). The contribution to the signal from the amorphous C support film may account for the dominant signature of  $\sigma^*$  type bonds. On the other hand,  $C=C \pi^*$  peaks can indicate the presence of aromatic rings and unsaturated bonds of hydrocarbons (contamination) typically present in the carbon films used to support TEM samples. Also,  $C=C \pi^*$  peaks can originate from unsaturated bonds that remain in the PPAA deposition, as  $C=C$  bonds are present in allylamine ( $CH_2=CH-CH_2-NH_2$ ); corresponding to incomplete polymerization of the allylamine. Therefore, it is necessary to use an alternative approach to determine the origin of the  $C=C \pi^*$  signal, for example using low-loss EFTEM in order to map the characteristic energy-loss peak of  $\sim 7$  eV that has been assigned to an electronic  $\pi-\pi^*$  transition of aromatic C rings (Li and Egerton, 2004).

Fig. 2a shows representative examples of high-resolution TEM images of Au@PPAA NPs with cores of different size. Extended electron irradiation resulted in tearing of the C support film, permitting clear visualization of NP shells for core sizes down to 1 nm. The shells typically have thicknesses of 1–2 nm and do not enclose the NPs uniformly. Fig. 2b shows the particle size distribution (PSD) measured from 216 NPs by applying a semi-automated segmentation algorithm (Gontard et al., 2011) to the image shown in Fig. 1. The PSD indicates that the Au cores have sizes of between 0.9 and 8 nm, with an average value of 2.25 nm and a standard deviation of 1.09 nm.

Fig. 2c shows a high-resolution TEM image of a hybrid NP with a core size of 1.5 nm attached to the edge of the C support. Fig. 2d shows a simulated high-resolution TEM image obtained from the atomistic model shown in Fig. 2e, which has a 1.5 nm Au core and an amorphous shell made of 75% C and 25% N. The contrast in the simulated image matches that in the experimental image qualitatively. The replacement of N atoms in the model by C atoms did not result in a substantial change in the simulated image, confirming the lack of sensitivity of high-resolution TEM to chemical changes for small differences in atomic number ( $Z=6$  for C and  $Z=7$  for N). The bright rim around the Au core in the simulation in Fig. 2d is associated with the fact that in the model there is a gap between the core and the shell. The absence of such a bright rim in the experimental image suggests that the core is capped coherently by the PPAA. The bright rim on the surface of the shell is consistent with the defocus value of +90 nm used in the simulation.

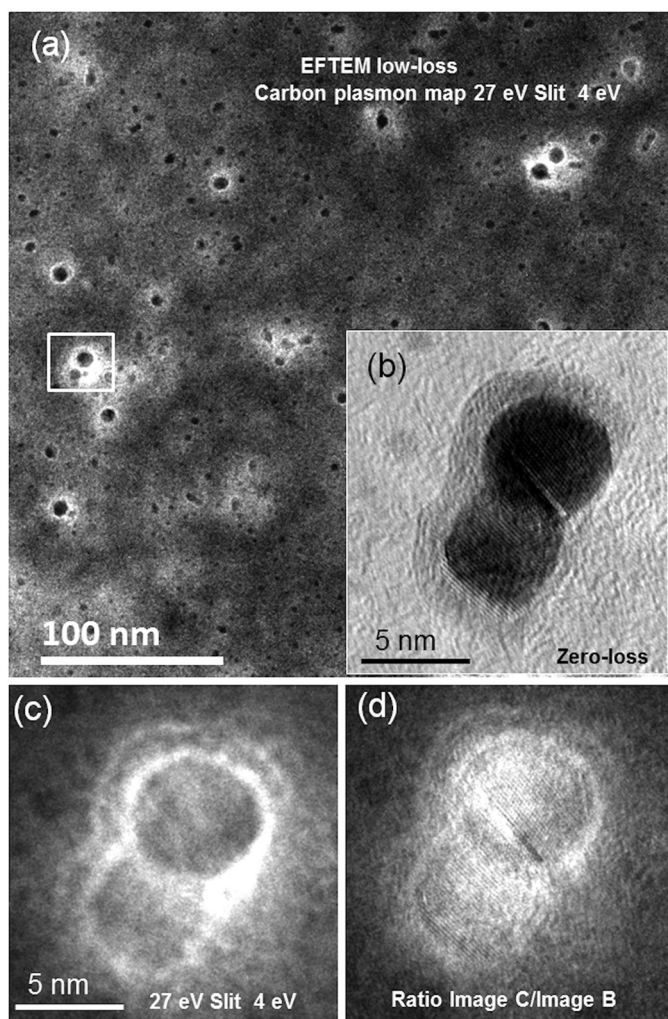
Fig. 3a shows a low-loss EFTEM image acquired from the specimen shown in Fig. 1 at an energy loss of 27 eV, which is close to the bulk plasmon energy expected for C that contains short-range (graphitic) order. Fig. 3b and c shows zero-loss and low-loss images, respectively, of two interacting particles indicated by a white square in Fig. 3a. Fig. 3d shows a ratio of the two images. The gray levels provide a measure of the plasmon excitation probability at a given position in the image integrated over the width of the energy window (Stöckli et al., 2000). The ratio image indicates that the plasmon resonances are particularly intense at the Au core, the Au-shell interface and the outer surface of the shell.

Fig. 4 illustrates the effect of the electron beam on the specimen. During TEM observation, the C support film thinned progressively until holes formed. Some NPs that were close to each other coalesced or changed in shape, while the shells around the NPs



**Fig. 2.** (a) Examples of high-resolution TEM images of Au@PPAA nanoparticles with cores of different size supported on thin C. (b) Measured particle size distribution of the Au cores (mean = 2.25 nm and SD = 1.09 nm). (c) High-resolution TEM image of a hybrid nanoparticle with a 1.5 nm core attached to the edge of the C support. (d) Simulated high-resolution TEM image intensity calculated using the atomistic model shown in (e). The model has a 1.5 nm Au core and an amorphous shell that contains 75% C and 25% N.

changed dramatically. Fig. 4a and the corresponding diffractograms below it show the evolution of two large NPs (numbered 5 in Fig. 5), which fused into one particle and became enclosed by a common shell. The first image in the sequence shows two Au NPs that are in contact and surrounded by an amorphous PPAA layer. The second image shows that the particles start to coalesce and that a common shell is created around both particles. The shell is now crystalline with  $\sim 6$  independent graphene-like layers with two different interplanar spacings visible in two directions. The first spacing of 0.33 nm is similar to the  $c$ -axis spacing between graphene sheets in graphite of 0.34 nm. The second spacing of 0.37 nm is similar to that reported for graphene/C shells surrounding Au NPs synthesized using chemical vapor deposition (Chopra et al., 2009). In the third image, the two NPs have fused together and the shell is now damaged. It is remarkable that the NPs were able to coalesce under intense electron beam irradiation while retaining the shell around them. In a related experiment, Au has been observed to flow between defective graphene particles (Sun et al., 2008). The image sequences in Fig. 4b illustrate the same



**Fig. 3.** (a) EFTEM image acquired in the low-energy-loss range for bulk plasmons using a 4 eV energy-selecting slit centered on an energy loss of 27 eV, which is close to the bulk plasmon energy for C with short-range (graphitic) order and also of Au ( $\sim 25$  eV). (b) Zero-loss image of a dimer of interacting Au NPs indicated with a white square in (a). (c) Low-loss image of the particles shown in (b). (d) Ratio of image (c) divided by image (b). The gray levels in (d) provide a direct measure of the plasmon excitation probability at a given position in the image integrated over the energy window. The plasmon resonances are particularly intense in the particles, at the Au-shell interface, in the contact region between the Au particles and at the outermost surface of the shell.

irradiation-induced transition in other particles (numbered 3 in Fig. 5). Fig. 4c–e shows simulations of the expected number of inelastic events (shown in pink) generated by the impact of 100 electrons accelerated by 60 V, 20 kV and 300 kV, respectively. For 60 V, the yield is 1 and the inelastic events remain at the surface. For 20 kV, the yield decreases but the “damage” affects the entire volume of the specimen. For 300 kV, the number of inelastic events is smaller than for 20 kV.

In order to confirm that the organic shell is PPAA, we used EFTEM to measure the presence and local distribution of N, which is a constituent of allylamine, with high spatial resolution. Images were acquired at a time when the PPAA coating had already started to be damaged by the electron beam. Fig. 5a shows a zero-loss EFTEM image recorded from “area 1” indicated in Fig. 1. Fig. 5b and c shows core loss EFTEM images acquired at the N K-edge (401 eV). Although specimen drift and/or damage will have affected parts of the background-subtracted elemental maps shown in Fig. 5b and c, the results are strongly suggestive of the presence of N around the Au NPs.

## 4. Discussion

We first discuss the possible origin of the high contrast features in the low-loss EFTEM images shown in Fig. 3. Second, we analyze the effects of electron irradiation on the integrity of the specimen. Third, we assess the phase transformations that occur after prolonged electron irradiation, including crystallization and amorphization.

### 4.1. EFTEM contrast: bulk or surface plasmons?

In Fig. 3, the high recorded intensity at the Au-PPAA interface and at the outermost surface of the capping layer is likely to be associated with the excitation of plasmons in the shell and/or the Au core. The images were recorded at an energy loss of 27 eV. For a Au NP, the bulk plasmon energy is typically  $\sim 25$  eV, although the precise value can depend on the nature of the surface and the oxidation state (Tsivadze et al., 2013). Surface plasmons can also be excited at the Au core, but they are typically observed in the optical range near 530 nm or 2.3 eV. Both theoretically and experimentally, shifts of surface plasmon energies in NPs have been shown to depend on the electronic properties of the particles. However, such energy shifts are mostly blue-shifts and their magnitudes rarely exceed 10 eV (Jain et al., 2007; Haridas et al., 2008). Hence, a shift of the surface plasmon energy of the Au core is not likely to be the source of the strong intensity in the shells observed in Fig. 3.

The bulk plasmon energy for C is between 22 and 27 eV, depending on the degree of short-range order present. For graphitic structures, the electronic properties and hence the plasmon energies in directions parallel and perpendicular to the graphitic shells are different (Stöckli et al., 2000). In some cases, surface plasmon excitation probabilities for nanotubes have resulted in the excitation of higher order surface plasmon resonance modes above 10 eV due to the finite lengths of the nanostructures, which impose a lower bound on the wave vector transfer of the electrons that excites the plasmons (Stöckli et al., 2000).

Given the different possible contributions to the strong contrast observed in Fig. 3, we are forced to conclude that we do not yet have a clear interpretation of its origin, which is likely to include the role of interfaces and electric charge. The energy losses in Fig. 3 are in the expected range for bulk plasmon excitations in Au and C, but their spatial distribution is not distributed uniformly, suggesting that the detailed morphology of the core-shell dimer in Fig. 3b and the structure and role of the support must be taken into account for a full interpretation of the contrast (Wang and Cowley, 1987). Oscillations of surface charges depend sensitively on the dielectric properties of the material and, more importantly, on the geometrical configuration of the interfaces. For example, energy losses of 20 eV have been measured using X-ray photoelectron spectroscopy at the surfaces of amorphous C films with superficial “polymeric-like” monolayer grafting (Godet et al., 2009). This signal was understood to originate from surface plasmons in the C layer, rather than from bulk losses in the “polymeric” grafting. Similarly, the higher probability of energy losses found at the interfaces of the particles in Fig. 3 may be associated with bulk plasmons originating from the capping layer.

### 4.2. Electron irradiation damage

The supporting C film thinned down and the PPAA shell amorphized and damaged after long exposure to the electron beam. At the accelerating voltage used in the present experiments, knock-on damage, *i.e.*, the displacement of an atom from its original site by the impact of the energetic electron beam, is inevitable. Of particular relevance is the loss of atoms that are expelled into vacuum (sputtered) from the specimen exit surface. The probability of knock-on

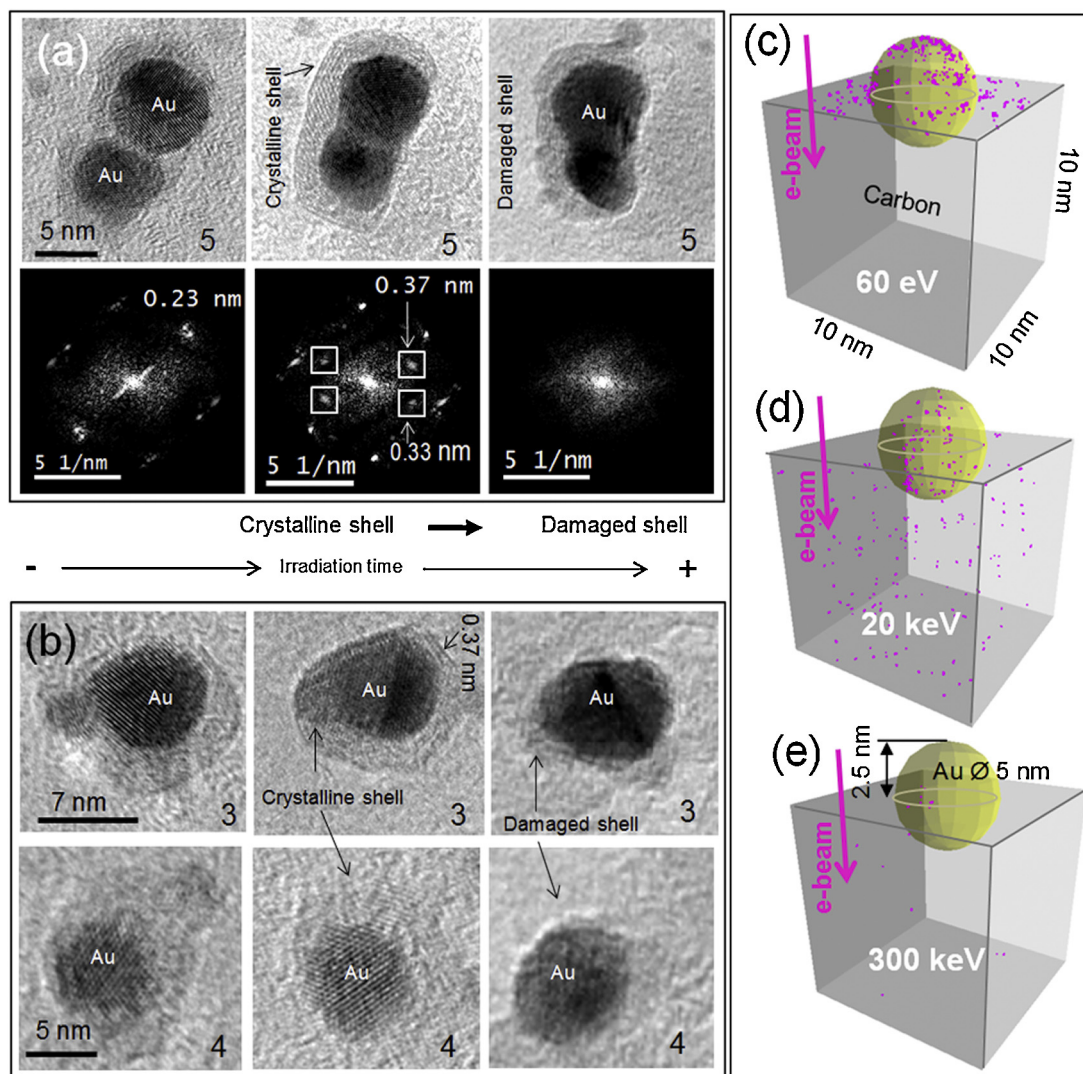


**Fig. 4.** Illustration of the effect of the electron beam on the specimen. After TEM observation, the C support film thinned down and subsequently holes opened across it. The process started slowly and then accelerated. Some particles that were close to each other coalesced or changed shape, while the shells surrounding the NPs underwent dramatic transformations. (a) High-resolution TEM images and corresponding diffractograms showing the evolution of two large particles that fused into one particle and became enclosed by a common graphitic shell. (b) Example of the transformation of a shell into a crystalline form. (c–e) Monte Carlo simulations of inelastic interactions (pink spots) generated by 60 eV, 20 keV and 300 keV electrons irradiating a 5 nm Au nanoparticle semi-buried in amorphous C. (For interpretation of the references to color in this figure legend, the reader is referred to the web version of the article.)

damage decreases with increasing atomic number and is therefore less likely for Au than for H, C, O or N. Despite the noticeable transformation of the hybrid NPs (Fig. 4), we measured the presence of N in their shells after 2 min of electron irradiation (Fig. 5) even after the shell became amorphous. Just as coating one or both surfaces of a specimen with C can help to preserve its crystallinity and to reduce mass loss, the presence of a C support film may have prevented sputtering of light atoms or other molecules from the organic shells into vacuum (Egerton et al., 2004). One proposed explanation is that a return to the original molecular state (healing of the broken bond) of an organic molecule is more likely if the escape of volatile elements is prevented (Fryer and Holland, 1983).

Another important source of damage in organic compounds is inelastic damage caused by valence electron (rather than core-loss) excitation. Even relatively radiation-resistant organic materials may undergo some form of damage when examined in an electron microscope at energies below the knock-on threshold energy. It is interesting to note that holes frequently formed close to NPs. The simulation in Fig. 4e indicates that at 300 keV inelastic events are more likely to happen in the Au NPs than in C. Hence, the

breaking of C–C bonds by radiolysis may soften the C film near the particles, enhancing the sputtering rate of C atoms. Another form of radiation-induced damage is through heat dissipation following energy transfer in inelastic events. Also, the electron beam can break hydrocarbon residues and typically result in a polymerization process that can frequently cover areas of the sample under study, degrading the quality of data acquired. Although the electron-beam-induced rise in specimen temperature is expected to be low for the experimental conditions used here (Li and Egerton, 2004), molecular dynamics simulations have shown that hole formation in thin C films can occur when the electron beam causes small clusters of amorphous C (e.g., from hydrocarbon contamination) to undergo thermal explosions (Börner et al., 2012).

A more profound consequence of inelastic scattering is that it leads to chemical changes in the specimen induced by the generation of low-energy (secondary) electrons. The specimen was irradiated with a high current flux (25 A/cm<sup>2</sup>), well above the critical electron dose for damage of PPAA, approximately  $0.9 \times 10^{-2}$  C/cm<sup>2</sup>, based on its melting temperature, (216 °C) (Kumar and Adams, 1990). For example, the images shown in the

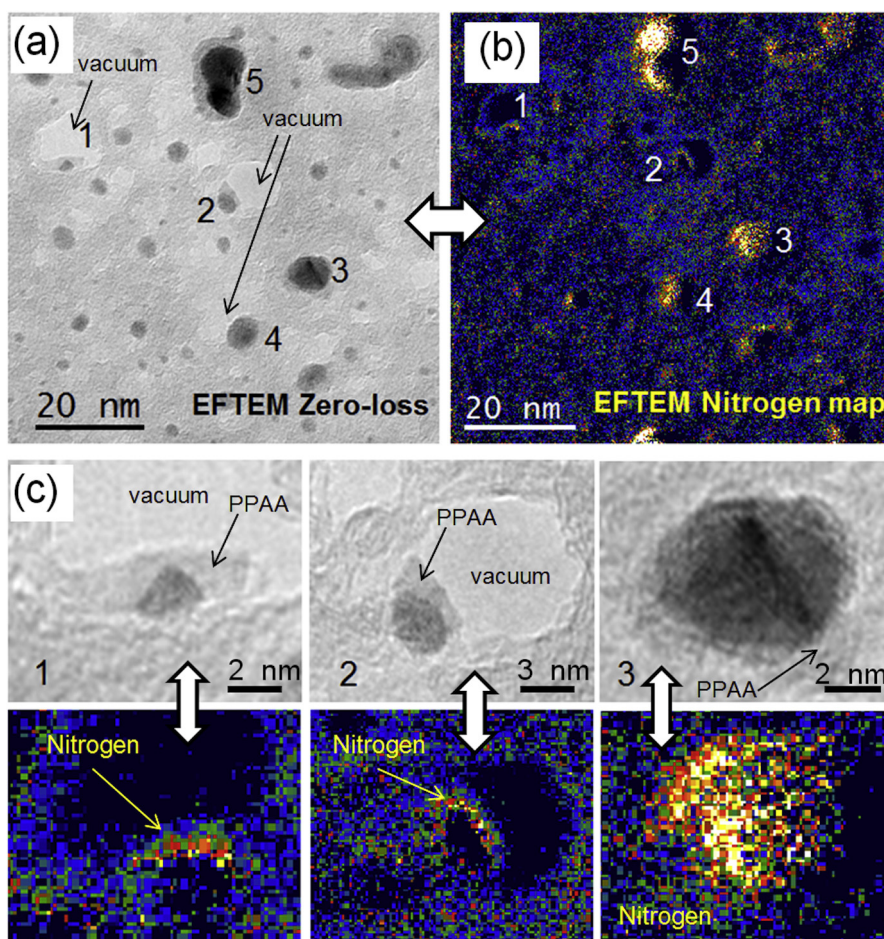


**Fig. 5.** (a) Zero-loss EFTEM image of “Area 1” indicated in Fig. 1. After 2 min of irradiation with 200 keV electrons (total dose =  $3 \times 10^3$  C/cm<sup>2</sup>), the C film became noticeably thinner and holes formed. (b) Background-subtracted N EFTEM elemental map. (c) Details of zero-loss images and N maps of three particles in (a) and (b). Although specimen drift and/or specimen damage may have affected parts of the elemental maps shown in (b) and (c), the results are suggestive of the presence of N associated with the positions of the Au particles.

Figs. 4 and 5 were acquired after exposures of 2 min, resulting in a total dose of  $3 \times 10^3$  C/cm<sup>2</sup>. Low-energy electrons that are produced by irradiation with high-energy particles may cause primary chain breakage and other molecular fragmentation, as well as the formation of double bonds and cross-linking (Sanche, 2002; Waske et al., 2012). Secondary electrons have low energies (usually below 70 eV) and thermalization distances on the order of nm, which define the initial volumes for energy deposition. Considering the stronger generation of secondary electrons in Au than in C, a polymer-metal interface of a hybrid NP is likely to be very vulnerable to radiation damage. Experiments on PPAA have demonstrated that amine groups (CN) remain stable during irradiation with low-energy (1–60 eV) electrons at low doses and that the primary chemical modifications are a loss of H and O (surface deoxidation) (Massey et al., 2010). Emission thresholds for cations and anions in irradiated PPAA were found to be between 7 and 25 eV, which is within the range of energies of secondary electrons and collective-excitations (inter band, intra band and plasmon resonances) generated by high-energy electron irradiation (Li and Egerton, 2004; Inada et al., 2011). The electron-induced decomposition of adsorbed organic layers with amine (NH<sub>2</sub>) groups on Au substrates has been observed to be initiated by secondary electrons, transforming the layer into an amorphous carbon nitride thin film (Wnuk et al., 2009). Monte Carlo simulations (see Fig. 4) show that for 60 eV incident electrons the yield of inelastic events is 1 and that they occur mainly at the surface of the sample. In our experiments,

irradiation was performed using 300 keV electrons, which have a much higher penetration depth (see Fig. 4), generating inelastic events inside the volume of the specimen and not only on its surface. For our experimental specimen thickness and incident electron energy, we calculated a yield for inelastic collisions of 5% of the number of incoming electrons. Even after applying a correction for the yield, the high current fluxes used in our experiments were several orders of magnitude higher than those used by Massey et al. (2010), indicating that the generation of a large number of secondary electrons is likely to have contributed to damage of the PPAA shells of our NPs.

#### 4.3. Electron-irradiation-induced crystallization

Figs. 4 and 5 show a phase transition suffered by the organic capping of the Au@PPAA NPs, first by a re-ordering of the layers and then by amorphization and subsequent damage. In particular, the formation of graphite-like layers was observed. Although Au is a noble metal that is typically not able to catalyze the formation of C-based materials, the growth of C shells in the vicinity of Au NPs has been observed *in situ* in the TEM. Graphene fragments and layers formed, suggesting that a crystalline Au surface can catalyze and provide a template for the ordering and crystallization of C. Moreover, under intense electron irradiation (50 A/cm<sup>2</sup>), the graphene fragments can close and form regular symmetric layers around the NPs until complete shell closure is achieved (Sutter et al., 2005).

However, the latter experiments were carried out at a specimen temperature of 550 °C, while the experiments shown here were carried out at room temperature.

Electron-induced graphitization of C is a well-known phenomenon, arising from cross-linking between neighboring molecules at low temperature. As a result of different hybridization, C is able to form different allotropes, of which graphite and diamond are the most well known (Banhart, 1999; Shakerzadeh et al., 2012). In particular, high-energy electron irradiation can graphitize free-standing amorphous C and form C anions (spherical structures with no dangling bonds that have a uniform strain distribution) (Börrnert et al., 2012). The graphitization (formation of C–C bonds) in polystyrene and PPAA as a result of irradiation with low-energy electrons has been observed (Massey et al., 2010; Lee et al., 2008), in addition to the loss of O and H. After prolonged irradiation, we observed that the PPAA shells were damaged, but we still measured the presence of N using EFTEM. Therefore, we can conclude that after crystallization C and N remained in the shells of the NPs in our specimen. The substitution of C by N in graphite in a regular fashion may have resulted in the formation of a “carbon nitride” (e.g., C<sub>3</sub>N<sub>4</sub>, C<sub>3</sub>N<sub>2</sub>, C<sub>3</sub>N, C<sub>5</sub>N or C<sub>10</sub>N<sub>3</sub>), or even graphitic g-C<sub>3</sub>N<sub>4</sub> (Thomas et al., 2008). Subsequent electron-beam-induced decomposition may therefore have transformed the layer into an amorphous carbon nitride, as previously reported for 1,2-diaminopropane films irradiated with electrons (Wnuk et al., 2009).

## 5. Conclusions

We have undertaken a TEM investigation of hybrid (metal/polymer) Au NPs capped with PPAA, which are of interest for applications in nanomedicine, such as selective targeting of tumor sites. Our results show that the PPAA coatings of unstained hybrid Au NPs can be imaged in the TEM with sufficient contrast at an accelerating voltage of 300 kV at ambient temperature without the need for staining. The thickness of the PPAA capping was typically below 2 nm and often non-uniform.

Features in EEL spectra are likely to be dominated by the signal from the C support film. This issue might be alleviated in a future study by using an impregnation technique for supporting the colloid of hybrid nanoparticles (Gontard et al., 2014b). EFTEM images recorded in the bulk plasmon energy regime showed strong intensity at the Au–polymer interface and at the external surface of the polymer shell. Qualitatively, the results presented here show that low-loss EFTEM can be an efficient source of high contrast in images of hybrid nanostructures. However, the full interpretation of such images requires further work because the plasmon modes of hybrid core–shell NPs cannot be treated as additive individual contributions of the core and shell modes (Chuntonov et al., 2012) and are very sensitive to small changes in local morphology and electrical state (Su et al., 2012; Jiang et al., 2014).

Whereas PPAA is predicted to be electron-beam-resistant at low doses, the PPAA layers of hybrid NPs damaged and became amorphous under electron beam irradiation at 300 keV when high doses were used, although we could still measure the presence of N in the shells. Knock-on damage is high at the accelerating voltages used in our work. However, the use of a C support film may reduce sputtering from the shells and explain their stability. On the other hand, Monte Carlo simulations show that the number of inelastic events close to the particles increases at low acceleration voltages ( $\leq 20$  kV). In a future study, it will be of great interest to compare the present results with images acquired at an intermediate accelerating voltage (60–80 kV).

Before the shells were destroyed, we observed the formation of crystalline order around larger NPs, as well as graphitic planes. Polymeric shells containing nitrogen were observed after

irradiation with very high electron doses, indicating that the particles are likely to be more stable at the relatively lower doses used in biomedical applications. Also, such experiments involving *in situ* TEM irradiation of polymers may be important for understanding electron-beam-induced structural changes in polymers and for refining approaches for tuning the optical properties of NPs. For example, polystyrene homopolymer films have been shown to become luminescent in visible light under 50 keV electron irradiation, which induced the re-formation of aromatic rings (Lee et al., 2008).

## Acknowledgment

We are grateful to the European Union for support under project reference REGPOT-CT-2011-285895-AI-NANOFUNC and under Grant Agreement 312483 – ESTEEM2 (Integrated Infrastructure Initiative – I3).

## References

- Banhart, F., 1999. Irradiation effects in carbon nanostructures. *Rep. Prog. Phys.* **62**, 1181–1221.
- Bawarski, W.E., Chidlow, E., Bharali, D.J., Mousa, S.A., 2008. Emerging nanopharmaceuticals. *Nanotechnology* **4**, 273–282.
- Börrnert, F., Avdoshenko, S.M., Bachmatiuk, A., Ibrahim, A., Büchner, B., Cuniberti, G., Rummeli, M.H., 2012. Amorphous carbon under 80 kV electron irradiation: a means to make or break graphene. *Adv. Mater.* **24** (41), 5630–5635.
- Chen, C., Daniel, M.C., Quinkert, Z.T., De, M., Stein, B., Bowman, V.D., Chipman, P.R., Rotello, V.M., Kao, C.C., Dragnea, B., 2006. Nanoparticle-templated assembly of viral protein cages. *Nano Lett.* **6** (4), 611–615.
- Chopra, N., Bachas, L.G., Knecht, M.R., 2009. Fabrication and biofunctionalization of carbon-encapsulated Au nanoparticles. *Chem. Mater.* **21**, 1176–1178.
- Chuntonov, L., Bar-Sadan, M., Houben, L., Haran, G., 2012. Correlating electron tomography and plasmon spectroscopy of single noble metal core–shell nanoparticles. *Nano Lett.* **12**, 145–150.
- Daniels, H.R., Brydson, R., Brown, A., Rand, B., 2003. Quantitative valence plasmon mapping in the TEM: viewing physical properties at the nanoscale. *Ultramicroscopy* **96**, 547–558.
- Demers, H., Poirier-Demers, N., Couture, A.R., Joly, D., Guilmain, L., De Jonge, N., Drouin, D., 2011. Three-dimensional electron microscopy simulation with the CASINO Monte Carlo software. *Scanning* **133**, 135–146.
- Drummy, L.F., Yang, J., Martin, D.C., 2004. Low-voltage electron microscopy of polymer and organic molecular thin films. *Ultramicroscopy* **99**, 247–256.
- Du Chesne, A., 1999. Energy filtering transmission electron microscopy of polymers – benefit and limitations of the method. *Macromol. Chem. Phys.* **200**, 1813–1830.
- Egerton, R.F., Li, P., Malac, M., 2004. Radiation damage in the TEM and SEM. *Micron* **35**, 399–409.
- Fryer, J.R., Holland, F., 1983. The reduction of radiation damage in the electron microscope. *Ultramicroscopy* **11**, 67–70.
- Garvie, L.A.J., Buseck, P.R., 2004. Nanosized carbon-rich grains in carbonaceous chondrite meteorites. *Earth Planet. Sci. Lett.* **224**, 431–439.
- Gittins, D.I., Caruso, F., 2001. Tailoring the polyelectrolyte coating of metal nanoparticles. *J. Phys. Chem. B* **105**, 6846–6852.
- Godet, C., David, D., Sabbah, H., Ababou-Girard, S., Solal, F., 2009. Bulk and surface plasmon excitations in amorphous carbon measured by core-level photoelectron spectroscopy. *Appl. Surf. Sci.* **255**, 6598–6606.
- Gontard, L.C., Knappett, B.R., Wheatley, A.E.H., Chang, S.L.-Y., Fernández, A., 2014a. Impregnation of carbon black for the examination of colloids using TEM. *Carbon* **76**, 464–468.
- Gontard, L.C., Moldovan, G., Carmona-Galán, R., Lin, C., Kirkland, A.I., 2014b. Detecting single-electron events in TEM using low-cost electronics and a silicon strip sensor. *Microscopy* **63** (2), 119–130.
- Gontard, L.C., Ozkaya, D., Dunin-Borkowski, R.E., 2011. A simple algorithm for measuring particle size distributions on an uneven background from TEM images. *Ultramicroscopy* **111**, 101–106.
- Haridas, M., Srivastava, S., Basu, J.K., 2008. Tunable variation of optical properties of polymer capped gold nanoparticles. *Eur. Phys. J. D* **49**, 93–100.
- Horiuchi, S., Hanada, T., Ebisawa, M., Matsuda, Y., Kobayashi, M., Takahara, A., 2009. Contamination-free transmission electron microscopy for high-resolution carbon elemental mapping of polymers. *ACS Nano* **3** (5), 1297–1304.
- Howie, A., 2003. Valence excitations in electron microscopy: resolved and unresolved issues. *Micron* **34**, 121–125.
- Hunt, J.A., Disko, M.M., Behal, S.K., Leapman, R.D., 1995. Electron energy-loss chemical imaging of polymer phases. *Ultramicroscopy* **58**, 55–64.
- Jain, P.K., Huang, X., El-Sayed, I.H., El-Sayed, M.A., 2007. Review of some interesting surface plasmon resonance-enhanced properties of noble metal nanoparticles and their applications to biosystems. *Plasmonics* **2**, 107–118.
- Jiang, N., Shao, L., Wang, J., 2014. (Gold nanorod core)/(polyaniline shell) plasmonic switches with large plasmon shifts and modulation depths. *Adv. Mater.* <http://dx.doi.org/10.1002/adma.201305905>.

- Kang, Y., Taton, T.A., 2005. Controlling shell thickness in core-shell gold nanoparticles via surface-templated adsorption of block copolymer surfactants. *Macromolecules* 38, 6115–6121.
- Karmani, L., Labar, D., Valembos, V., Bouchat, V., Nagaswaran, P.G., Bol, A., Gillart, J., Levêque, P., Bouzin, C., Bonifazi, D., Michiels, C., Feron, O., Grégoire, V., Lucas, S., Borght, T.V., Gallez, B., 2013. Antibody-functionalized nanoparticles for imaging cancer: influence of conjugation to gold nanoparticles on the biodistribution of <sup>89</sup>Zr-labeled Cetuximab in mice. *Contrast Media Mol. Imag.* 8, 402–408.
- Katrinak, K.A., Rez, P., Buseck, P.R., 1992. Structural variations in individual carbonaceous particles from an urban aerosol. *Environ. Sci. Technol.* 26, 1967–1976.
- Krivanek, O.J., Dellby, N., Murfitt, M.F., Chisholm, M.F., Pennycook, T.J., Suenaga, K., Nicolosi, V., 2010. Gentle STEM: ADF imaging and EELS at low primary energies. *Ultramicroscopy* 110, 935–945.
- Kumar, S., Adams, W.W., 1990. Electron beam damage in high temperature polymers. *Polymer* 31, 15–19.
- Inada, H., Su, D., Egerton, R.F., Konno, M., Wu, L., Ciston, J., Wall, J., Zhu, Y., 2011. Atomic imaging using secondary electrons in a scanning transmission electron microscope: experimental observations and possible mechanisms. *Ultramicroscopy* 111, 865–876.
- Lee, H.M., Kim, Y.N., Kim, B.H., Kim, S.O., Cho, S.O., 2008. Fabrication of luminescent nanoarchitectures by electron irradiation of polystyrene. *Adv. Mater.* 20, 2094–2098.
- Li, D., He, Q., Li, J., 2009. Smart core/shell nanocomposites: intelligent polymers modified gold nanoparticles. *Adv. Colloid Interface Sci.* 149, 28–38.
- Li, P., Egerton, R.F., 2004. Radiation damage in coronene, rubrene and p-terphenyl, measured for incident electrons of kinetic energy between 100 and 200 keV. *Ultramicroscopy* 101, 161–172.
- Libera, M.R., Egerton, R.F., 2010. Advances in the transmission electron microscopy of polymers. *Polym. Rev.* 50 (3), 321–339.
- Linares, E.M., Leite, C.A.P., Valadares, L.F., Silva, C.A., Rezende, C.A., Galembeck, F., 2009. Molecular mapping by low-energy-loss energy-filtered transmission electron microscopy imaging. *Anal. Chem.* 81, 2317–2324.
- Malac, M., Beleggia, M., Egerton, R., Zhu, Y., 2007. Bright-field TEM imaging of single molecules: dream or near future? *Ultramicroscopy* 107, 40–49.
- Marega, R., Karmani, L., Flamant, L., Nageswaran, P.G., Valembos, V., Masereel, B., Feron, O., Borght, T.V., Lucas, S., Michiels, C., Gallez, B., Bonifazi, D., 2012. Antibody-functionalized polymer-coated gold nanoparticles targeting cancer cells: an in vitro and in vivo study. *J. Mater. Chem.* 22, 21305–21312.
- Martin, D.C., Chen, J., Yang, L.F., Drummy, L.F., Kübel, C., 2005. High resolution electron microscopy of ordered polymers and organic molecular crystals: recent developments and future possibilities. *J. Polym. Sci. B: Polym. Phys.* 43, 1749–1778.
- Masereel, B., Dinguizli, M., Bouzin, C., Moniotte, N., Feron, O., Gallez, B., Borght, T.V., Michiels, C., Lucas, S., 2011. Antibody immobilization on gold nanoparticles coated layer-by-layer with polyelectrolytes. *J. Nanopart. Res.* 13, 1573–1580.
- Massey, S., Gallino, E., Cloutier, P., Tatoulian, M., Sanche, L., Mantovani, D., Roy, D., 2010. Low-energy electrons and X-ray irradiation effects on plasma-polymerized allylamine bioactive coatings for stents. *Polym. Degrad. Stab.* 95, 153–163.
- Moreau, N., Michiels, C., Masereel, B., Feron, O., Gallez, B., Borght, T.V., Lucas, S., 2009. PVD synthesis and transfer into water-based solutions of functionalized gold nanoparticles. *Plasma Process. Polym.* 6 (S1), 888–892.
- Müller, H., Jin, J., Danev, R., Spence, J., Padmore, H., Glaeser, R.M., 2010. Design of an electron microscope phase plate using a focused continuous-wave laser. *New J. Phys.* 12, 073011.
- Nagayama, K., Danev, R., 2008. Phase contrast electron microscopy: development of thin-film phase plates and biological applications. *Phil. Trans. R. Soc. B* 363, 2153–2162.
- Nelayah, J., Gu, L., Sigle, W., Koch, C.T., Pastoriza-Santos, I., Liz-Marzán, L.M., van Aken, P.A., 2009. Direct imaging of surface plasmon resonances on single triangular silver nanoprism at optical wavelength using low-loss EFTEM imaging. *Opt. Lett.* 34 (7), 1003–1005.
- Sardar, R., Park, J.-W., Shumaker-Parry, J.S., 2007. Polymer-induced synthesis of stable gold and silver nanoparticles and subsequent ligand exchange in water. *Langmuir* 23, 11883–11889.
- Sanche, L., 2002. Nanoscopic aspects of radiobiological damage: fragmentation induced by secondary low-energy electrons. *Mass Spectrom. Rev.* 21, 349–369.
- Shakerzadeh, M., Loh, G.C., Xu, N., Chow, W.L., Tan, C.W., Lu, C., Yap, R.C.C., Tan, D., Tsang, S.H., Teo, E.H.T., Tay, B.K., 2012. Re-ordering chaotic carbon: origins and application of textured carbon. *Adv. Mater.* 24, 4112–4123.
- Stöckli, T., Bonard, J.-M., Châtelain, A., Wang, Z.L., Stadelmann, P., 2000. Plasmon excitations in graphitic carbon spheres measured by EELS. *Phys. Rev. B* 61 (8), 5751–5759.
- Su, H., Zhong, Y., Ming, T., Wang, J., Wong, K.M., 2012. Extraordinary surface plasmon coupled emission using core/shell gold nanorods. *J. Phys. Chem. C* 116, 9259–9264.
- Sun, L., Krashennnikov, A.V., Ahlgren, T., Nordlund, K., Banhart, F., 2008. Plastic deformation of single nanometer-sized crystals. *Phys. Rev. Lett.* 101, 156101.
- Sutter, E., Sutter, P., Zhu, Y., 2005. Assembly and interaction of Au/C core-shell nanostructures: in situ observation in the transmission electron microscope. *Nano Lett.* 5 (19), 2092–2096.
- Thomas, A., Fischer, A., Goettmann, F., Antonietti, M., Müller, J.-O., Schlögl, R., Carlsson, J.M., 2008. Graphitic carbon nitride materials: variation of structure and morphology and their use as metal-free catalysts. *J. Mater. Chem.* 18, 4893–4908.
- Tsivadze, A.Y., Ionova, G.V., Mikhalko, V.K., Ionova, I.S., Gerasimov, G.A., 2013. The fine structure of plasmon bands in gold nanoparticles. *Prot. Met. Phys. Chem. Surf.* 49 (2), 166–168.
- van Schooneveld, M.M., Gloter, A., Stephan, O., Zagonel, L.F., Koole, R., Meijerink, A., Mulder, W.J.M., de Groot, F.M.F., 2010. Imaging and quantifying the morphology of an organic-inorganic nanoparticle at the sub-nanometre level. *Nat. Nanotechnol.* 5, 538–544.
- Wang, Z.L., Cowley, J.M., 1987. Surface plasmon excitation for supported metal particles. *Ultramicroscopy* 21, 77–94.
- Waske, P.A., Meyerbröker, N., Eck, W., Zharnikov, M., 2012. Self-assembled monolayers of cyclic aliphatic thiols and their reaction toward electron irradiation. *J. Phys. Chem. C* 116, 13559–13568.
- Wnuk, J.D., Gorham, J.M., Fairbrother, D.H., 2009. Growth and microstructure of nanoscale amorphous carbon nitride films deposited by electron beam irradiation of 1,2-diaminopropane. *J. Phys. Chem. C* 113, 12345–12354.